Digital Image Inpainting Analysis Based on the Cahn-Hilliard Model

Nada S. AL-Fartosi and Ahmed K. Al-Jaberi
Mathematics Department, College of Education for Pure Science, the University of Basrah, 61001 Basrah, Iraq
nada.sarhan@uobasrah.edu.iq, ahmed.shanan@uobasrah.edu.iq

Keywords: Image Inpainting, Cahn-Hilliard Model, Color Spaces, Image Quality Assessment, Finite Difference Method.

Abstract: One of the most important applications in image processing is digital image restoration, which attempts to restore sections of an image that have been lost or damaged. In this paper, we analyze and implement the Cahn-Hilliard model, a fourth-order nonlinear partial differential equation renowned for its efficiency and speed in preserving structural continuity and smoothness in the image. The model is designed to restore regions affected by intentional damage, scratches, or distortions. The model was numerically solved using the implicit finite difference method, which produced a stable and precise reconstruction using the convex partitioning technique. We applied the model to images with deliberate defects within eight different color spaces, including YUV, YCbCr, RGB, NTSC, XYZ, HSV, and others, and evaluated its performance in terms of restoration accuracy and the absence of visual distortions. The effectiveness of the Cahn-Hilliard model outperforms traditional restoration methods in reconstructing missing areas while preserving the original edges and fine details.

1 INTRODUCTION

A fundamental problem in digital image processing is the reconstruction of absent or impaired areas within an image by utilizing information derived from adjacent pixels. This technique, known as inpainting, serves as a specific type of interpolation. Furthermore, it facilitates the restoration of compromised photographs impacted by elements like aging, scratches, deterioration, or deliberate harm. Furthermore, inpainting can facilitate the recoloring of occluded objects by recreating the concealed information utilizing contextual clues [1]. Bretozzi was the pioneer in presenting a two-scale analytical model derived from the Cahn-Hilliard equation, which has demonstrated efficacy in the processing of binary images, especially those consisting solely of two hues (black and white). The Cahn-Hilliard framework, initially developed as a physical and mathematical model, has been effectively modified for image processing applications, particularly image inpainting, owing to its superior efficiency and rapidity in managing high-contrast images [2] - [4]. Bertozzi further advanced an extended model, known as the Bertozzi-Esedoglu-Gillette Cahn-Hilliard model, to accommodate images with n channels. Bertozzi and her partners specifically created a fidelity term to guarantee that the inpainted image closely resembles the original before purposeful damage or noise. The extended model exhibits robust mathematical and numerical performance; yet, it encounters a critical issue: the compromise of mass conservation, which pertains to maintaining the spatial average of the phase field [5]. Researchers continue to strive to address this constraint, particularly in ensuring mass conservation when incorporating the fidelity term. A recent study by Nils Boulerion proposed optimal control strategies for the fidelity parameter that balance inpainting accuracy and mass preservation [6], [7]. The study conducted by Bretozzi, Cecilia, Matteo, and M. Grasselli focuses on an image inpainting model that was initially presented by A. Bretozzi and associates, which is based on a Cahn-Hilliard-type partial differential equation. This model regulates the progression of an order parameter $u \in [0,1]$, which approximates the original image specified over a confined, two-dimensional domain Ω [8]. Carrillo, Kalliadasis, Liang, and Perez assessed the usefulness of utilizing a modified Cahn-Hilliard inpainting filter for inputting damaged images into a classification neural network. Utilizing the Modified National Institute of Standards Technology (MNIST) dataset, their findings indicate

that this methodology markedly enhances prediction accuracy by as much as 50% in certain instances, particularly for low to moderate damage levels [9]. Dandan Jiang, Mejdi Azaiez, Alain Miranville, and Chuahju Xu suggested an upgraded Cahn-Hilliard-type inpainting model using a nonlocal diffusion operator. This model exhibits exceptional efficacy in rebuilding absent areas in photographs [10]. Anis Mohamed, Hamdi Houichet, and Anis Theljani used the Cahn-Hilliard equation to devise an efficient method for inpainting binary images, concentrating on the restoration of low-order structures, including edges and corners, and the augmentation of image borders. The numerical results demonstrate the model's accuracy in attaining objectives [11]. Martin, Lin, and Carola introduced a novel paradigm in image processing, namely binary image refinement utilizing the Cahn-Hilliard equation. They examined the equilibrium state of the model and introduced a generalization for grayscale images with constrained contrast. They achieved a structural refinement of images distinguished by a smooth curving of the gradient levels [12]. Qiumei, Jiaxuan, and Zhen introduced a mass-preserving adaptive time-scaling model for Physics-Informed Neural Network (PINN) that dynamically segments the time domain based on the energy decay rate. This model addressed the Cahn-Hilliard equations with an autonomous neural network, and the outcomes illustrated the efficacy of this technique [13].

Jessica and Martin devised a model employing the vector-valued Cahn-Hilliard equation. Numerical examples illustrate that the sanctioned fractional Cahn-Hilliard method of interior mapping surpasses its non-fractional counterpart, enhancing the signal-to-noise ratio and structure similarity index. Experiments validate that the suggested model is comparable to prior interior mapping techniques, including total variance and fourth-order variable interior mapping methods [14]. Antun, Darko, and Anderj proposed a novel nonlocal partial differential equation derived from the Cahn-Hilliard model for the purpose of image restoration. The suggested linear model exhibits lower computational costs compared to the Cahn-Hilliard equation while still delivering high-quality interior painting outcomes. An example of internal coloring was presented to demonstrate the method's possibilities [15]. Qing Zou introduced a fourth-order partial differential equation model for picture coloration, integrating the Perona-Malik and Cahn-Hilliard equations through the principle of energy partitioning.

The numerical results indicate that the suggested model demonstrates superior colorization performance with reduced calculation time relative to traditional PDE models [16]. Despite the extensive application of the Cahn-Hilliard equation in binary image inpainting, comprehensive research examining its performance over many color spaces and comparing its efficacy among various color models remains insufficient. The classical Cahn-Hilliard model is adopted due to its well-established physical and mathematical foundation, which enables rigorous analytical treatment and clear energy estimates. This choice allows us to isolate the effect of the color space representation without introducing additional nonlocal complexities. Although nonlocal Cahn-Hilliard extensions exist and are physically relevant, they are beyond the scope of the present work.This paper examines the application of the Cahn-Hilliard model across multiple color spaces (CMY, YCbCr, RGB, YUV, XYZ, NTSC, HSL, and HSV) as seen in [17], evaluates the visual analysis of the resultant images, and assesses their quality through statistical metrics including mean square error (MSE), peak signal-to-noise ratio (PSNR), structural similarity (SSIM) and entropy [18]. The rest of the paper is organized as follows: Section 2 elucidates the digital images. Section 3 introduces the concept of picture inpainting. Section 4 reviews color spaces and their suitability for Cahn-Hilliard image modeling. Section 5 presents the Cahn-Hilliard model. Section 6 presents and discusses several numerical results of the proposed model. Section 7 will present the conclusion.

2 DIGITAL IMAGE

A two-dimensional digital image is made up of a certain set of digital values, which are pixels. In an image, each pixel has a unique location x_{ij} and is linked to an intensity number d(x_{ij}) which tells you about the color, and as a number, each value in the image ranges from 0 to 255, with 0 being the least intense and 255 being the most intense. Each pixel in a greyscale image has a single intensity number that ranges from 0 (black) to 255 (white). When talking about color images, the RGB (red, green, and blue) color range is usually used. According to the specified model, each pixel in a color image has three numerical values, one from 0 to 255, which represent the strengths of the red, green, and blue parts [19].

3 IMAGE INPAINTING

Image inpainting is the process of using information from the surrounding field to recreate missing or damaged areas of an image so that the viewer is unaware of the changes [20]. The size and nature of the missing areas have a significant impact on this method's effectiveness. The visual result is better when the inpainting zone is smaller and the surrounding texture is simpler. The inpainting technique relies heavily on texture, which represents the regularity, smoothness, and coarseness of image parts. When damage arises from intentional scratching, ageing, or weathering, images can be effectively restored [21]. However, reconstruction becomes more difficult when a significant portion of the image is missing because the remaining portions do not provide essential contextual information.

4 COLOR SPACES

Color spaces are mathematical constructs that represent colors as numerical values, each tailored for certain uses such as image reduction, broadcasting, and picture restoration. They are typically classified into two categories: those that utilize primary channels directly, such as RGB and CMY, and those that differentiate luminance and chrominance, including YCbCr, YUV, HSV, HIS, and XYZ. In RGB, each channel has completed structural and chromatic information, potentially leading to discrepancies when channels are handled separately. In contrast, YCbCr and YUV separate luminance (Y) from chrominance (Cb, Cr), hence augmenting compression efficiency and strengthening edge preservation [22]. HSV and HSL offer a perceptually intuitive depiction of hue, saturation, and value, closely correlating with human color perception; nonetheless, they exhibit instabilities in the hue axis when saturation is absent [23]. The XYZ model provides a linear depiction of the spectrum and underpins perceptual models such as (CIE-Commission International de I'E`clairage) CIELAB, although it lacks perceptual uniformity. CIELAB is not perceptually uniform [24].

The suitability of the Cahn-Hillird model depends on how different color space representations capture image structures and perceptual consistency. In the Y channel of YCbCr, the model enhances edge integrity and diminishes noise; however, in RGB, it may result in inconsistencies among R, G, and B due to the independent processing of channels. The efficacy of inpainting is significantly influenced by the selection of color space: RGB is optimal for display, YCbCr/YUV for compression and restoration, HSV/HSL for perceptual design, and XYZ for scientific applications necessitating spectral accuracy [9].

5 MODIFIED CAHN-HILLIARD MODEL

One semi-linear fourth-order partial differential equation (PDE) developed for binary image inpainting is the modified Cahn-Hilliard (mCH) equation [3]. The field of material sciences uses this equation [24]. with $\vec{x} = (x, y)$ and let D⊂Ω represent the inpainting domain; let f($\vec{x}$) be a specified image defined throughout the domain Ω. The resolution of (1) under Neumann boundary conditions is employed to restore the compromised images. The implicit finite difference method is utilized to solve (1), while the convex partition of (6) and (7) is employed to provide numerical stability. The equation is given by:

$$\partial_t u = \Delta\left(-\epsilon\,\Delta u - \frac{1}{\epsilon}F(u)\right) + \lambda(\vec{x})(f(\vec{x}) - u), \quad \text{in } \Omega \quad (1)$$

$$\text{Where } (\vec{x}) = \begin{cases} 0 & if\ \vec{x} \in D \\ \lambda_0 & if\ \vec{x} \in \Omega \backslash D \end{cases}$$

Equation (1) is known as the mCH equation, and it includes an additional fidelity term $\lambda(\vec{x})\,(f(\vec{x}) - u)$. The function $F(u)$ is referred to as a double-well potential, given by $F(u) = 1/u(1-u)^2$, and ϵ is a tiny positive parameter that approaches zero. To solve (1), it is sufficient to minimize the following energy functions:

$$\int_\Omega \left(\frac{\epsilon}{2}|\nabla u|^2 + \frac{1}{\epsilon}f(u)\right) d\vec{x} + \lambda_0 \int_{\Omega\backslash D}(f-u)^2 d\vec{x}. \quad (2)$$

The initial component denotes the energy of a gradient flow based on the H^{-1}-norm, resulting in the mCH equation, whereas the subsequent component is a fidelity term derived from a gradient flow utilizing the L^2-norm. This process is similar to the convexity splitting used in an isotropic framework. Diffusion inpainting functions under a fourth-order total variation framework. The fitting term represents a gradient flow in $H^{-1}(\Omega)$. The fitting term represents a gradient flow in $H^{-1}(\Omega)$. The fidelity term is considered on $L^2(\Omega)$. In this context, $H^{-1}(\Omega)$ is the dual Sobolev space of $H_0^1(\Omega)$, with the associated norm defined as:

$$\|f\|_{-1}^2 = \|\nabla\Delta^{-1}f\|_{-1}^2 = \int_\Omega (\nabla\Delta^{-1})^2 d\vec{x} \quad (3)$$

Where Δ^{-1}refers to the inverse of the Laplace operator, such that $u = \Delta^{-1}f$ is $-\Delta u = f$ in Ω, with $u = 0$ on $\partial\Omega$. Let:

$$R_1 = \int_\Omega \left(\frac{\epsilon}{2}|\nabla u|^2 + \frac{1}{\epsilon}F(u)\right) d\vec{x}, \quad (4)$$

$$R_2 = \lambda_0 \int_{\Omega\setminus D} (f-u)^2 d\vec{x} \quad (5)$$

Convexity splitting is applied separately to R_1 and R_2 decomposed as:

Where $R_1 = R_{11} - R_{12}$, then

$$R_{11} = \int_\Omega \left(\frac{\epsilon}{2}|\nabla u|^2 + \frac{C_1}{2}|u|^2\right) d\vec{x}, \quad (6)$$

$$R_{12} = \int_\Omega \left(-\frac{1}{\epsilon} + F(u) + \frac{C_1}{2}|u|^2\right) d\vec{x} \quad (7)$$

Likewise $R_2 = R_{21} - R_{22}$, where:

$$R_{21} = \int_{\Omega\setminus D} \frac{C_2}{2}|u|^2 d\vec{x}, \quad (8)$$

$$R_{22} = \int_{\Omega\setminus D} (-\lambda_0(f-u)^2) + \frac{C_2}{2}|u|^2 d\vec{x} \quad (9)$$

Based on the above, the resulting time-stepping scheme is given by:

$$\frac{u^{n+1}-u^n}{k} + \epsilon\nabla^4 u^{n+1} - C_1\nabla^2 u^{n+1} + C_2 u^{n+1} = \nabla^2\left(\frac{1}{\epsilon}f'(u^n) + \lambda(\vec{x})(f(\vec{x}) - u^n)\right) - C_1\nabla^2 u^n + C_2 u^n \quad (10)$$

We enforce Neumann boundary conditions on $\partial\Omega$. $\nabla U_{k+1}.\vec{n} = \nabla\Delta U_{k+1}.\vec{n} = 0$, ($\frac{\partial u}{\partial n} = 0$, $\frac{\partial(\Delta u)}{\partial u} = 0$), on $\partial\Omega$.

The significance of this model lies in its ability to restore large missing regions without introducing artefacts [3]. The overall workflow of the proposed Cahn-Hilliard inpainting process is summarized in Figure 1, which illustrates the sequential steps from initialization, application of the modified PDE, convexity splitting, to the final image reconstruction.

6 NUMERICAL EXPERIMENTS AND RESULTS

The proposed Cahn-Hilliard model was implemented on 80 color images from the Berkeley Color Database [25], which includes high-texture color images. As shown in Figure 2, two experiments were conducted using the model and color spaces described earlier.

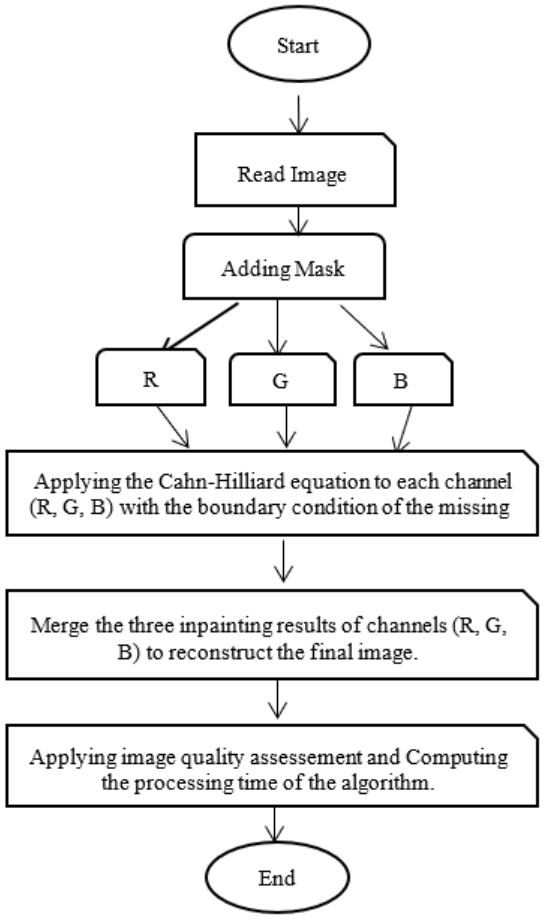

Figure 1: Flowchart of inpainting process using Cahn-Hilliard.

Figure 2: Example of four out of 300 trained natural images.

The process of image inpainting may be explained in the following way: $D \subset \Omega$ stands for the inpainting domain, $f: \Omega \longrightarrow R^{+1}$ for the specified image, and Ω for the image domain. Binary masks were used to create four instances of intrinsic

inpainting domains, which are damaged regions, in the image. Here is an equation that shows scratches and text may be added to the original image: f is the original image, M is the mask image, and M^{-1} is the logical inverse of the mask image.

$$f_{Damaged} = M^{-1}(x,y) \times f(x,y) + M\,(x,y). \quad (11)$$

As illustrated in Figure 3, the masks were selected based on the breadth of M, the scratches; specifically, the first two masks illustrate scratches of varying widths, which indicate minor damaged areas. The third mask depicts a big scratch, indicating vast damaged areas. Lastly, the fourth mask includes two missing blocks. The four masks will be applied to a series of high-texture, natural-colored photographs, as previously stated. To replace each image's missing parts, we will put the Cahn-Hilliard model into practice. After that, we use Structural quality measures (SQMs), including structural similarity indices (SSIM) [26], peak signal-to-noise ratio (PSNR) [27], mean square error (MSE) [28], and the information entropy of both the input image (E_0) and the output image E_1. To visually and statistically compare the experiment outcomes.

These SQMs are used to evaluate the model's efficiency in terms of its ability to retrieve missing regions from the image. The time taken to obtain results was also studied, and the image recovery was implemented in MATLAB code (elapsed for MATLAB R2020a, running on a laptop with an Intel (R) Core (TM) i7-9850H CPU at 2.60 GHz and 32 GB of RAM). Two experiments were conducted in this section. Section 6.1 presents an experiment analyzing the model's behavior on missing regions of different sizes; Section 6.2 presents an experiment analyzing the model's behavior on different numbers of iterations.

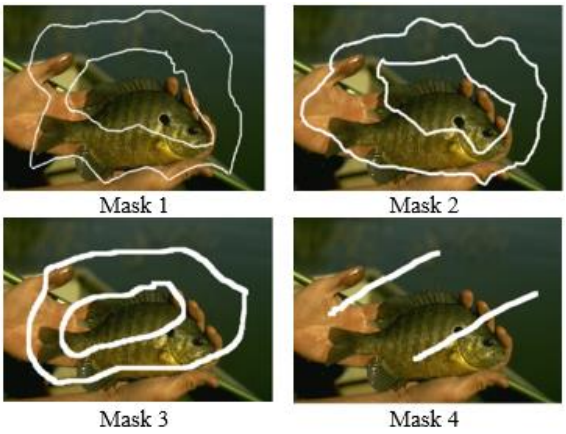

Figure 3: Illustrates the types of image masks, each with different missing areas.

6.1 Different Types of Missing Areas

In this section, four experiments were conducted, and their results were presented in four tables. Four different masks were adopted, representing different levels of damage in the images, with each mask varying in the area of the deleted region. To achieve the accuracy and stability of the results, processing was performed using a different iteration for each mask. These experiments were applied to images after converting them to eight different color spaces. The goal was to evaluate the model's performance across multiple color contexts and determine the color space that offers the best performance. The color space performance was correlated with the damage level (mask) to determine whether the mask type directly affects the effectiveness of the color space. And as shown in the Tables 1 - 4.

Table 1: The average values of MSE, PSNR, SSIM, and entropy for image inpainting using the Cahn-Hilliard equation in MASK 1 at iteration 50.

SPACES	MSE	PSNR	SSIM	E_0	E_1	Time(s)
YCbCr	129.4358	28.52194	0.996911	7.150389	7.132853	3.2793
YUV	129.4525	28.5211	0.996911	7.150389	7.132865	3.7909
NTSC	129.4564	28.5203	0.996916	7.150389	7.132804	3.401
CMY	129.5468	28.51616	0.996911	7.150389	7.132109	3.2976
RGB	129.5593	28.51598	0.996913	7.150389	7.132185	4.3965
HSL	133.7117	28.33284	0.996784	7.150389	7.132971	3.4191
XYZ	140.2804	28.13715	0.996444	7.150389	7.145394	3.6312
HSV	146.3791	27.59021	0.996544	7.150389	7.140073	3.3785

Table 2: The average scores of MSE, PSNR, SSIM, and entropy for filling in the image using the Cahn-Hilliard equation in MASK 2 after 100 iterations.

SPACES	MSE	PSNR	SSIM	E_0	E_1	Time(s)
RGB	238.6114	25.70954	0.994181	7.150389	7.132164	5.8563
CMY	238.6429	25.70864	0.994174	7.150389	7.132075	5.8694
NTSC	238.6943	25.70794	0.99418	7.150389	7.132924	5.9029
YUV	238.9249	25.70575	0.994165	7.150389	7.133233	6.282
YCbCr	238.9501	25.70566	0.994164	7.150389	7.13319	5.9514
HSL	245.7121	25.55883	0.993996	7.150389	7.133219	5.8508
XYZ	251.0125	25.45771	0.993522	7.150389	7.145744	5.9259
HSV	262.6121	25.1639	0.993749	7.150389	7.139844	5.751

Table 3: The mean values of MSE, PSNR, SSIM, and entropy for image inpainting using the Cahn-Hilliard equation in MASK 3 at iteration 250.

SPACES	MSE	PSNR	SSIM	E_0	E_1	Time(s)
CMY	444.3194	22.74889	0.977894	7.150389	7.13198	14.0398
RGB	445.7759	22.7349	0.977957	7.150389	7.134693	14.0332
NTSC	446.0363	22.73104	0.977948	7.150389	7.137225	13.342
YCbCr	448.1505	22.70714	0.977899	7.150389	7.139373	13.8648
YUV	448.2783	22.70618	0.977893	7.150389	7.139736	14.2992
HSL	468.6999	22.46513	0.977565	7.150389	7.136658	16.7154
HSV	481.466	22.35831	0.977296	7.150389	7.14076	13.48
XYZ	490.6576	22.22118	0.975891	7.150389	7.151723	13.9947

Table 4: The average scores for MSE, PSNR, SSIM, and entropy for image inpainting using the Cahn-Hilliard equation in MASK 4 at iteration 300.

SPACES	MSE	PSNR	SSIM	E_0	E_1	Time(s)
CMY	442.0186	23.05999	0.991994	7.150389	7.132155	19.1881
RGB	443.626	23.03534	0.992016	7.150389	7.133326	16.5651
NTSC	444.3275	23.0302	0.992009	7.150389	7.134341	16.5168
YUV	446.0074	23.00626	0.992	7.150389	7.135559	17.0714
YCbCr	446.0081	23.0061	0.991999	7.150389	7.13534	16.5636
HSL	468.3886	22.76904	0.991785	7.150389	7.134586	18.7603
XYZ	477.9063	22.64644	0.991507	7.150389	7.14782	16.4762
HSV	483.4296	22.6306	0.991736	7.150389	7.141024	16.3957

The first experiment involved 50 iterations of the numerical operation on a small erased region (Table 1). The color spaces are arranged from best to worst according to the MSE values. YCbCr achieved the best reconstruction accuracy, exhibiting the lowest MSE. In terms of other image quality metrics (PSNR and SSIM), NTSC, YCbCr, and YUV outperformed HSV, HSL, and XYZ. However, the maximum entropy (7.145394) was observed in XYZ, indicating higher information diversity or noise. Regarding computational time, RGB and YUV were the slowest, whereas CMY and YCbCr were the fastest.

The results after 100 iterations are summarized in Table 2. Again, the color spaces are ranked according to MSE. The best MSE, PSNR, and SSIM were obtained in RGB, while HSV was the fastest despite having the worst MSE and PSNR. XYZ exhibited the highest entropy (7.145744).

In Table 3, 250 iterations were performed on a large missing region (mask 3). CMY achieved the best MSE and PSNR, whereas RGB had the highest SSIM. The weakest performance was observed for XYZ. NTSC was the fastest, and HSL the slowest. Among all spaces, XYZ showed the smallest difference between Entr1 and Entr0.

Table 4 presents results for 300 iterations. CMY again had the best MSE and PSNR, while HSV performed the worst. RGB achieved the highest SSIM, and XYZ had the lowest entropy.

Based on these experiments, RGB demonstrated the best overall performance in terms of numerical accuracy (MSE), perceptual quality (PSNR, SSIM), and structural similarity. Figure 4 illustrates examples of restored images for four masks in the RGB space.

6.2 Different Iterations of Numerical Solutions

In this section, we conducted eight experiments across a variety of color spaces. We studied the behavior of the model for four different mask sizes, each with its unique size. For each mask, we performed four different iterations, each varying from one mask to another. The experimental results were evaluated using a set of statistical metrics. The goal of the experiment was to determine the relationship between the number of iterations, the mask type and the performance of color spaces to achieve the best restoration quality while, calculating execution time to ensure acceptable time efficiency. The adopted iterations for the masks were in the first mask (1, 10, 20, 50); in the second mask (1, 25, 50, 100); in the third mask (50, 100, 150, 250); and finally in the fourth mask (100, 150, 200, 300). Tables 5-8 show the experimental results for eight spaces. Figure 5 below illustrates the visual study of the outcomes in the RGB space for the restoration of ideal mask 1 across four iterations.

Table 5: The mean values of MSE, PSNR, SSIM, and entropy for image inpainting performed with the Cahn-Hilliard equation in eight spaces in MASK 1 at different iterations.

SPACES	Iteration	MSE	PSNR	SSIM	E_o	E_I	Time(s)
YCbCr	1	3165.246	13.50443	0.95616	7.150389	7.059599	1.0179
	10	341.7871	23.07316	0.988663	7.150389	7.170919	1.4241
	20	143.4894	27.72096	0.996074	7.150389	7.13996	1.8428
	50	129.4358	28.52194	0.996911	7.150389	7.132853	3.3896
YUV	1	3720.908	12.75597	0.952901	7.150389	7.063469	1.26605
	10	341.5751	23.07634	0.988666	7.150389	7.72933	1.7073
	20	143.5141	27.72095	0.996073	7.150389	7.140531	2.2896
	50	129.4525	28.5211	0.996911	7.150389	7.132865	3.7909
NTSC	1	1264.155	17.58749	0.973349	7.150389	7.031703	0.9002
	10	311.6674	23.54745	0.989584	7.150389	7.166328	1.3387
	20	141.748	27.81553	0.996169	7.150389	7.138831	1.8634
	50	129.4564	28.5203	0.996916	7.150389	7.132804	3.3378
CMY	1	3016.431	13.78254	0.938621	7.150389	6.923821	0.9024
	10	258.1104	24.57675	0.994465	7.150389	7.131321	1.3112
	20	138.8738	27.97146	0.99669	7.150389	7.132268	1.8128
	50	129.5468	28.51616	0.996911	7.150389	7.132109	3.2976
RGB	1	4877.128	11.43425	0.947441	7.150389	6.999926	0.8949
	10	304.252	23.64348	0.989634	7.150389	7.145318	1.3348
	20	141.6216	27.82485	0.996171	7.150389	7.135334	1.8143
	50	129.5593	28.51598	0.996913	7.150389	7.132185	4.3965
HSL	1	3298.814	13.13769	0.956141	7.150389	7.068999	0.9204
	10	449.4215	21.99576	0.986982	7.150389	7.155859	1.3773
	20	163.4075	26.98501	0.995595	7.150389	7.13779	1.8711
	50	133.7117	28.33284	0.996784	7.150389	7.132971	3.3483
XYZ	1	6823.633	10.02331	0.939318	7.150389	6.923334	1.0118
	10	784.4291	19.57025	0.97937	7.150389	7.174031	1.4384
	20	215.9553	25.59298	0.992207	7.150389	7.153446	1.9461
	50	140.2804	28.13715	0.996444	7.150389	7.145394	3.4367
HSV	1	1293.183	17.66026	0.974549	7.150389	6.995213	0.9032
	10	282.0068	24.07335	0.99104	7.150389	7.150298	1.3504
	20	146.3791	27.59021	0.996149	7.150389	7.142936	1.8748
	50	153.6056	27.7542	0.996544	7.150389	7.140073	3.3501

Table 6: The mean results of MSE, PSNR, SSIM, and entropy for image inpainting using the Cahn-Hilliard equation in eight spaces in MASK 2 at different iterations.

SPACES	Iteration	MSE	PSNR	SSIM	E_o	E_I	Time(s)
YCbCr	1	4402.113	12.07889	0.950719	7.150389	7.075903	1.7199
	25	400.845	22.51144	0.989096	7.150389	7.17589	2.1576
	50	245.0842	25.42381	0.993853	7.150389	7.139683	3.4039
	100	238.9501	25.70566	0.994164	7.150389	7.13319	5.9423
YUV	1	5230.198	11.28716	0.947083	7.150389	7.079419	2.4123
	25	400.6006	22.51483	0.989099	7.150389	7.177643	2.4492
	50	245.1169	25.42369	0.993852	7.150389	7.140273	3.6873
	100	238.9249	25.70575	0.994165	7.150389	7.133233	6.282
NTSC	1	1771.119	16.14835	0.968592	7.150389	7.075834	1.9118
	25	373.097	22.89856	0.989762	7.150389	7.167958	2.0869
	50	243.784	25.4708	0.9939	7.150389	7.137823	3.3001
	100	238.6943	25.70794	0.99418	7.150389	7.132924	5.9473
CMY	1	4695.988	11.85383	0.922636	7.150389	6.958289	1.671
	25	333.3885	23.57936	0.99286	7.150389	7.131619	2.0665
	50	243.3636	25.50248	0.99407	7.150389	7.131169	3.2999
	100	238.6429	25.70864	0.994174	7.150389	7.132075	5.8694
RGB	1	7494.983	9.57385	0.939702	7.150389	7.051214	1.219
	25	367.0325	22.97309	0.989799	7.150389	7.148879	2.0514
	50	243.6413	25.47474	0.993904	7.150389	7.134506	3.296
	100	238.6114	25.70954	0.994181	7.150389	7.132164	5.8563
HSL	1	5570.518	10.869	0.947689	7.150389	7.121845	1.8412
	25	516.3749	21.47701	0.98774	7.150389	7.158126	2.0881
	50	264.7761	24.96655	0.993505	7.150389	7.137085	3.3145
	100	245.7121	25.55883	0.993996	7.150389	7.133219	5.8641
XYZ	1	10034.86	8.347463	0.931651	7.150389	6.947726	2.3892
	25	816.8024	19.42884	0.981041	7.150389	7.18315	2.1833
	50	303.7746	24.22331	0.991181	7.150389	7.152949	3.4675
	100	251.0125	25.45771	0.993522	7.150389	7.145744	6.0226
HSV	1	1791.552	16.21623	0.969203	7.150389	7.05778	1.8365
	25	357.1924	23.13484	0.990605	7.150389	7.153898	2.1132
	50	253.8277	25.16754	0.993703	7.150389	7.14225	3.2635
	100	262.6121	25.1639	0.993749	7.150389	7.139844	5.8176

Figure 4: Examples of inpainting images. (a) Original images, (b) Mask images, (c) Inpainted images according to Cahn-Hilliard equation.

Table 7: The average measurements of MSE, PSNR, SSIM, and entropy for image inpainting using the Cahn-Hilliard equation in eight spaces in MASK 3 at different iterations.

SPACES	Iteration	MSE	PSNR	SSIM	E_o	E_I	Time(s)
YCbCr	50	1756.245	15.8466	0.959638	7.150389	7.271531	3.3461
	100	713.376	19.95439	0.971293	7.150389	7.202233	5.7492
	150	498.6449	21.91925	0.976028	7.150389	7.164529	8.6225
	250	448.1505	22.70714	0.977899	7.150389	7.139373	14.1383
YUV	50	1743.566	15.87916	0.959812	7.150389	7.268519	3.6137
	100	713.2994	19.95624	0.971299	7.150389	7.204938	6.1898
	150	498.6918	21.91908	0.976027	7.150389	7.166223	8.7557
	250	448.2783	22.70618	0.977893	7.150389	7.139736	14.2992
NTSC	50	1365.8	17.03396	0.961761	7.150389	7.234925	3.3647
	100	655.9176	20.37605	0.972177	7.150389	7.187393	5.7966
	150	483.805	22.10149	0.976392	7.150389	7.155629	8.4965
	250	446.0363	22.73104	0.977948	7.150389	7.137225	13.7396
CMY	50	1083.13	18.15948	0.96918	7.150389	7.133953	3.3231
	100	562.7513	21.25241	0.975637	7.150389	7.130045	5.8847
	150	462.9449	22.39461	0.977323	7.150389	7.130005	8.3085
	250	444.3194	22.74889	0.977894	7.150389	7.13198	14.0398
RGB	50	1482.098	16.59438	0.961832	7.150389	7.201906	3.2928
	100	648.3756	20.43904	0.972334	7.150389	7.1608	5.8797
	150	482.8686	22.11798	0.976422	7.150389	7.14397	8.2933
	250	445.7759	22.7349	0.977957	7.150389	7.134693	14.0332
HSL	50	1780.958	15.87768	0.959759	7.150389	7.224463	3.3677
	100	859.031	19.19395	0.970393	7.150389	7.170281	5.8478
	150	590.2388	21.08679	0.97516	7.150389	7.150425	8.4316
	250	468.6999	22.46513	0.977565	7.150389	7.136658	13.8891
XYZ	50	3089.263	13.52654	0.950154	7.150389	7.261341	3.4565
	100	1285.04	17.40549	0.963558	7.150389	7.201464	5.9382
	150	720.7941	20.09725	0.97071	7.150389	7.172338	8.2894
	250	490.6576	22.22118	0.975891	7.150389	7.151723	13.9795
HSV	50	911.0818	18.78756	0.967193	7.150389	7.189668	3.4545
	100	600.904	20.84083	0.973643	7.150389	7.159231	5.7921
	150	507.4896	21.82613	0.976241	7.150389	7.148503	8.4356
	250	481.466	22.35831	0.977296	7.150389	7.14076	13.6727

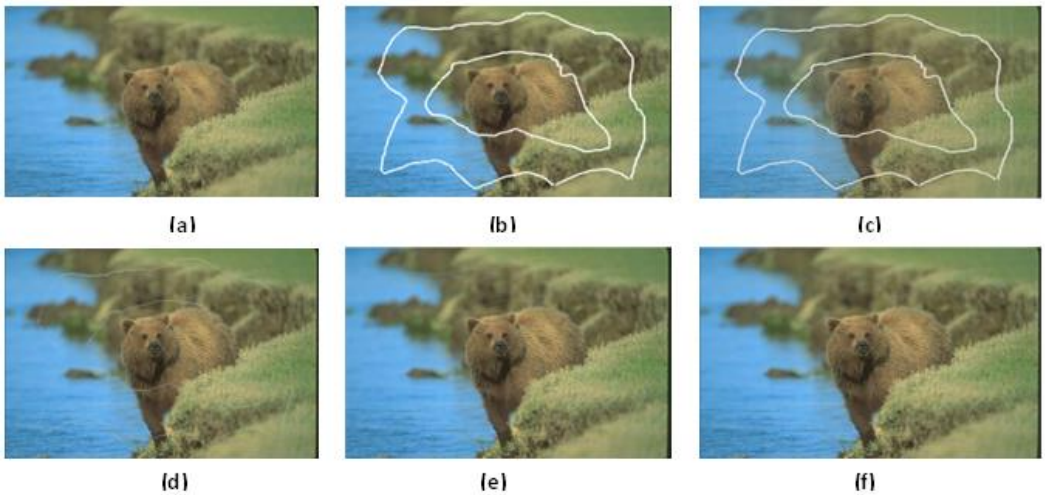

Figure 5: Examples of inpainting images: a) Original image, b) Mask image, c), d), e), and f) Inpainted images by Cahn-Hilliard when iterations are (1, 10, 20, and 50, respectively).

Table 8: The mean values of MSE, PSNR, SSIM, and entropy for image inpainting performed with the Cahn-Hilliard equation in eight spaces in MASK 4 at different iterations.

SPACES	Iteration	MSE	PSNR	SSIM	E_o	E_I	Time(s)
YCbCr	100	840.4149	19.24566	0.989036	7.150389	7.168335	6.0104
	150	542.0065	21.56051	0.990956	7.150389	7.15096	8.6905
	200	466.2394	22.58638	0.991713	7.150389	7.142035	11.1672
	300	446.0081	23.0061	0.991999	7.150389	7.13534	16.2808
YUV	100	840.4708	19.24901	0.989041	7.150389	7.16992	6.2791
	150	541.9464	21.56226	0.990959	7.150389	7.152089	8.6339
	200	466.2181	22.5857	0.991715	7.150389	7.142635	11.3377
	300	446.0074	23.00626	0.992	7.150389	7.135559	17.0714
NTSC	100	751.4746	19.79615	0.989409	7.150389	7.160778	5.9398
	150	515.7375	21.85865	0.991148	7.150389	7.146134	8.4854
	200	458.0235	22.71281	0.991782	7.150389	7.139135	11.2168
	300	444.3275	23.0302	0.992009	7.150389	7.134341	16.067
CMY	100	641.2911	20.78006	0.990752	7.150389	7.130641	5.6369
	150	483.525	22.33204	0.991614	7.150389	7.130373	8.4411
	200	447.3168	22.8912	0.991881	7.150389	7.130893	13.5895
	300	442.0186	23.05999	0.991994	7.150389	7.132155	19.1881
RGB	100	743.4341	19.85199	0.989515	7.150389	7.147591	5.787
	150	514.2454	21.8833	0.991171	7.150389	7.139859	8.4372
	200	457.7541	22.71671	0.991787	7.150389	7.135914	11.1094
	300	443.626	23.03534	0.992016	7.150389	7.133326	16.5651
HSL	100	991.0061	18.65478	0.988854	7.150389	7.151863	5.9125
	150	684.4718	20.51923	0.99049	7.150389	7.143669	8.5589
	200	533.1117	21.88933	0.991372	7.150389	7.138311	11.1309
	300	468.3886	22.76904	0.991785	7.150389	7.134586	16.4884
XYZ	100	1519.686	16.75016	0.986419	7.150389	7.173889	5.994
	150	838.7148	19.49555	0.989	7.150389	7.161115	8.5032
	200	592.1172	21.30653	0.990479	7.150389	7.153944	10.9898
	300	477.9063	22.64644	0.991507	7.150389	7.14782	16.5856
HSV	100	637.8425	20.6598	0.99027	7.150389	7.149519	5.8829
	150	537.2672	21.67579	0.991179	7.150389	7.145386	8.3959
	200	489.3065	22.35145	0.99159	7.150389	7.142779	11.0514
	300	483.4296	22.6306	0.991736	7.150389	7.141024	16.06

The above tables showed the final results as follows:

1) The first and second masks (Tables 1, 2) achieved the best performance when using the YCbCr space at 50 iterations and the RGB space at 100 iterations, where image reconstruction was high-resolution and relatively short [10]. This is due to the structural properties of the YCbCr and RGB spaces. The YCbCr space separates the image components into the luminance (Y) component and the color (Cb, Cr) components [29]. This separation is very useful for recovering small missing regions because it allows for more accurate and efficient processing [10]. The proposed Cahn-Hilliard model enables focusing on the important visual details in the Y channel while allowing some tolerance in the Cb and Cr color channels without affecting the quality of the recovered image. Therefore, this space is used in techniques (compression, restoration, etc.) [9]. Therefore, the RGB space requires a larger number of iterations (100) to improve accuracy [10].
2) In the third and fourth masks (Tables 3, 4), the CMY and RGB spaces achieved the best values in terms of MSE, PSNR, and SSIM. This is because the RGB and CMY color spaces represent colors directly, which allows for accurate reconstruction of large deleted areas. But they recorded the highest difference in entropy, indicating a significant amount of information change between the original and processed images, since the two spaces do not separate the lighting and color components. And because processing images in RGB and CMY spaces requires more calculations, it leads to increased execution time [30], [31].

3) The HSV space was approximately the fastest to execute, but it recorded poor results on the (MSE, PSNR, and SSIM) metrics. This is because the HSV space is primarily designed for color correction applications and not for pixel retrieval. Although it separates hue from value, this separation is not suitable for retrieving the original image structure. This renders it unfit for retrieving and enhancing high-resolution images, where image quality takes precedence over time [32]. The XYZ space had the lowest entropy difference of all the spaces, indicating that the image retained its information values after processing. The result may indicate that the changes did not significantly affect the image, and therefore, the XYZ space did not significantly improve it. This is because XYZ space is a theoretical color space designed to accurately represent colors according to the human visual model, without taking into account process ability or visual
enhancement [33].
4) We obtained lower MSE values and higher SSIM and PSNR; the execution time was faster in the first and second masks (Tables 5, 6). The Cahn-Hilliard equation can accurately retrieve the image because the surrounding pixels provide sufficient spatial and color information [9]. In contrast, the third and fourth masks had a large missing region (Tables 7, 8), so we required more time. We observed a significant increase in MSE values and a significant decrease in PSNR and SSIM values. The result indicates that the processed image differs significantly from the original image in terms of pixel values, structure, and visual content. This variation is because the retrieval algorithm lacks sufficient indifrom the original image, making it difficult to reconstruct structures and details, even with an increasing number of iterations (250, 300) [8].

7 CONCLUSIONS

The Cahn-Hilliard phase diffusion model was employed to reconstruct absent areas in images and was utilized across diverse images and configurations of missing regions. The proposed approach was executed in tests that encompassed many iterations and eight distinct color spaces. The findings indicated a strong correlation between the magnitude of the absent region and the number of iterations employed, since both influence the quality of retrieval. It was noted that small masks necessitated fewer iterations to attain satisfactory results, but masks with extensive missing areas demanded more iterations to acquire acceptable outcomes. The findings underscore the necessity of balancing the extent of the missing area, the iteration count, and the choice of a suitable color space to optimize future image retrieval. Based on the overall analysis of the results, it can be concluded that the model demonstrated stable preformance and several positive characteristics that confirm its effectiveness in image processing across different color spaces. The findings revealed that the selection of the color space has a direct impact on enhancing the quality of the reconstructed image and reducing numerical error, as the variation among spaces clarified the model's behavior toward spatial structure and color information. The experiments also showed that th interaction between the model and the missing regions depends on balancing visual properties and numerical accuracy.

REFERENCES

[1] C. Schönlieb and A. Bertozzi, “Unconditionally stable schemes for higher order inpainting,” Commun. Math. Sci., vol. 9, no. 2, pp. 413-457, 2011.

[2] A. Bertozzi, S. Esedoglu, and A. Gillette, “Analysis of a two-scale Cahn–Hilliard model for binary image inpainting,” Multiscale Model. Simul., vol. 6, no. 3, pp. 913-936, 2007.

[3] L. Bertozzi, S. Esedoglu, and A. Gillette, “Inpainting of binary images using the Cahn–Hilliard equation,” IEEE Trans. Image Process., vol. 16, no. 1, pp. 285-291, 2006.

[4] A. Al-Jaberi, S. A. Jassim, and N. Al-Jawad, “Inpainting large missing regions based on Seam Carving,” EAI Endorsed Trans. Ind. Networks Intell. Syst., vol. 5, no. 16, 2018.

[5] L. Cherfils, H. Fakih, and A. Miranville, “A Cahn–Hilliard system with a fidelity term for color image inpainting,” J. Math. Imaging Vis., vol. 54, pp. 117-131, 2016.

[6] N. Bullerjahn, “Error estimates for full discretization by an almost mass consEervation technique for Cahn–Hilliard systems with dynamic boundary conditions,” arXiv Prepr. arXiv2502.03847, 2025.

[7] A. K. Al-Jaberi, A. Asaad, S. A. Jassim, and N. Al-Jawad, “Topological data analysis to improve exemplar-based inpainting,” in Mobile Multimedia/Image Processing, Security, and Applications 2018, SPIE, 2018, pp. 13-24.

[8] E. Beretta, C. Cavaterra, M. Fornoni, and M. Grasselli, “Optimal control of the fidelity coefficient in a Cahn-Hilliard image inpai,” arXiv Prepr. arXiv2502.03025, 2025.

[9] J. A. Carrillo, S. Kalliadasis, F. Liang, and S. P. Perez, “Enhancement of damaged-image prediction through Cahn–Hilliard image inpainting,” R. Soc. Open Sci., vol. 8, no. 5, p. 201294, 2021.

[10] D. Jiang, M. Azaiez, A. Miranville, and C. Xu, “Nonlocal Cahn-Hilliard type model for image inpainting,” Comput. Math. with Appl., vol. 159, pp. 76-91, 2024.

[11] A. Theljani, H. Houichet, and A. Mohamed, “An adaptive Cahn-Hilliard equation for enhanced edges in binary image inpainting,” J. Algorithm. Comput. Technol., vol. 14, p. 1748302620941430, 2020.

[12] M. Burger, L. He, and C.-B. Schönlieb, “Cahn–Hilliard inpainting and a generalization for grayvalue images,” SIAM J. Imaging Sci., vol. 2, no. 4, pp. 1129-1167, 2009.

[13] H. Qiumei, M. Jiaxuan, and X. Zhen, “Mass-preserving Spatio-temporal adaptive PINN for Cahn-Hilliard equations with strong nonlinearity and singularity,” arXiv Prepr. arXiv2404.18054, 2024.

[14] J. Bosch and M. Stoll, “A fractional inpainting model based on the vector-valued Cahn–Hilliard equation,” SIAM J. Imaging Sci., vol. 8, no. 4, pp. 2352-2382, 2015.

[15] A. L. Brkić, D. Mitrović, and A. Novak, “On the image inpainting problem from the viewpoint of a nonlocal Cahn-Hilliard type equation,” J. Adv. Res., vol. 25, pp. 67-76, 2020.

[16] Q. Zou, “An image inpainting model based on the mixture of Perona–Malik equation and Cahn–Hilliard equation,” J. Appl. Math. Comput., vol. 66, no. 1, pp. 21-38, 2021.

[17] A. K. Al-Jaberi, S. A. Jassim, and N. Al-Jawad, “Colourizing monochrome images,” in Mobile Multimedia/Image Processing, Security, and Applications 2018, SPIE, 2018, pp. 25-37.

[18] Halim and B. V. R. Kumar, “An anisotropic PDE model for image inpainting,” Comput. Math. with Appl., vol. 79, no. 9, pp. 2701-2721, 2020.

[19] J. W. Cahn, “On spinodal decomposition,” Acta Metall., vol. 9, no. 9, pp. 795-801, 1961.

[20] J. W. Cahn, “On spinodal decomposition in cubic crystals,” Acta Metall., vol. 10, no. 3, pp. 179-183, 1962.

[21] J. W. Cahn and J. E. Hilliard, “Free energy of a nonuniform system. I. Interfacial free energy,” J. Chem. Phys., vol. 28, no. 2, pp. 258-267, 1958.

[22] Zhang, J. Tian, D. Li, X. Hou, and L. Wang, “An anisotropic PDE model for image inpainting photoplethysmography (IPPG) method,” Technol. Heal. Care, vol. 30, no. 1_suppl, pp. 391-402, 2022.

[23] M. D. Fairchild, “Color Appearance Models.”

[24] G. Sharma and R. Bala, Digital color imaging handbook, CRC Press, 2017.

[25] K. Cheng, W. Feng, C. Wang, and S. M. Wise, “An energy stable fourth order finite difference scheme for the Cahn–Hilliard equation,” J. Comput. Appl. Math., vol. 362, pp. 574-595, 2019.

[26] K. Gu, S. Wang, G. Zhai, W. Lin, X. Yang, and W. Zhang, “Analysis of distortion distribution for pooling in image quality prediction,” IEEE Trans. Broadcast., vol. 62, no. 2, pp. 446-456, 2016.

[27] A. C. Bovik, Handbook of image and video processing, Academic Press, 2010.

[28] Z. Wang, A. C. Bovik, H. R. Sheikh, and E. P. Simoncelli, “Image quality assessment: from error visibility to structural similarity,” IEEE Trans. Image Process., vol. 13, no. 4, pp. 600-612, 2004.

[29] T. Barbu, Digital Image Processing, Analysis and Computer Vision Using Nonlinear Partial Differential Equations, vol. 1211, Springer Nature, 2025.

[30] S. Prativadibhayankaram et al., “A study on the effect of color spaces in learned image compression,” in 2024 IEEE International Conference on Image Processing (ICIP), IEEE, 2024, pp. 3744-3750.

[31] X. He, Y. Liu, P. Beckett, H. Uddin, A. Nirmalathas, and R. R. Unnithan, “A new CMY camera technology using Al-TiO2-Al nanorod filter mosaic integrated on a CMOS image sensor,” arXiv Prepr. arXiv2010.11680, 2020.

[32] P. Hu, Y. Han, and J.-S. Pan, “An Advanced Bald Eagle Search Algorithm for Image Enhancement,” Comput. Mater. Contin., vol. 82, no. 3, 2025.

[33] A. Kerr, “The CIE XYZ and xyY color spaces,” Colorimetry, vol. 1, no. 1, pp. 1-16, 2010.